Contribution of Lakes in Sustaining Greening of the Sahara during the Mid-Holocene

Yuheng Li[1], Kanon Kino[1], Alexandre Cauquoin[2] and Taikan Oki[1]

[1]Department of Civil Engineering, Graduate School of Engineering, the University of Tokyo, Tokyo, Japan.
[2]Institute of Industrial Science, The University of Tokyo, Kashiwa, Japan.

Correspondence to: Yuheng Li (yuheng@rainbow.iis.u-tokyo.ac.jp)

Abstract. The contribution of lake-climate impact to sustain the Green Sahara in the mid-Holocene (MH, 6000 years ago) is still under debate. To assess the lake-induced climate response over North Africa, we investigated the roles of Western Sahara lakes and Megalake Chad using reconstructions of MH Sahara lake maps as surface boundary conditions for the isotope-enabled atmospheric model MIROC5-iso. Our results show that the Western Sahara lakes pushed the West African monsoon northward and extended it eastward by expanding Megalake Chad. Such lake-climate impact was caused by the cyclonic circulation response related to weakened African Easterly Jet and enhanced Tropical Easterly Jet. According to the Budyko aridity index, the northwestern Sahara climate region shifted from hyper-arid to arid or semi-arid with lake expansion. Moreover, precipitation scarcity could be reduced by up to 13% to sustain semi-humid conditions. Such lake-climate impact alleviates the Sahara aridity but relies on lake positions in the monsoon regions. Our findings are promising for understanding the contribution of lakes to sustaining the Green Sahara.

删除了: feedback

删除了: feedback

删除了: feedback

1 Introduction

Much paleoclimate evidence shows that in the mid-Holocene (MH, 6000 years ago), Sahara, the largest hot desert in the world, was much wetter and greener compared with the present-day climate (Gasse, 2000; Adkins, deMenocal, & Eshel, 2006; Claussen, M. et al., 2017). This period, called Green Sahara (GS) or African Humid Period (AHP), was mainly caused by the Earth's orbital cycle revolution on obliquity, eccentricity, and precession, leading to high seasonality insolation in the Northern Hemisphere (Otto-Bliesner et al., 2017) with approximately 7% higher summer insolation over North Africa (NAf) during the MH than today (Berger, 1988). Under such orbital forcing changes, the West African Monsoon (WAM) strengthened and extended northward, leading to distinct rainfall regimes and increased vegetation along with narrow desert zones in Sahara (Kutzbach et al., 2020). Although the GS climate is highly correlated with orbital forcing, state-of-the-art general circulation models (GCMs) cannot account for the widespread precipitation during the GS period (Braconnot et al., 2007; Perez-Sanz et al., 2014; Harrison et al., 2015; Brierley et al., 2020). Hence, researchers have investigated oceanic and terrestrial roles in sustaining the GS. Remote oceanic impact contributes to enhanced summer monsoon with increasing sea surface temperature (Braconnot et al., 1999; Kutzbach & Liu, 1997; Zhao et al., 2005) and winter rainfall (Cheddadi et al., 2021) over NAf. Further, the inland terrestrial system is affected by vegetation growth (Thompson et al., 2022), especially interactions with soil (Kutzbach et al., 1996; Chen et al., 2020), dust reductions (Messori et al., 2018), and dust-cloud interactions (Hopcroft & Valdes, 2019; Braconnot et al., 2021). Despite terrestrial and ocean improvements in the model modules and an understanding of their roles in the GS climate, the MH climate simulations from the Paleoclimate Modeling Intercomparison Project 4 (PMIP4) still underestimate the northward WAM extension (Brierley et al., 2020).

Despite implementing all terrestrial impact in model MH simulations, biases still exist in the contribution of open-water surfaces (lakes and wetlands) over NAf that are often set as the same as in pre-industrial control simulations. Hoelzmann et al. (1998) reconstructed the Megalake Chad distribution in the Sahara during the Holocene (hereinafter small-lake map; LK_98 in Tables 1 and S1). By adopting this small-lake map to the Community Climate Model version 3 (CCM3) climate model, Broström et al. (1998) and Carrington et al. (2001) found that Megalake Chad produced more localized hydrological changes and did not contribute to the northward WAM movement. Contrastingly, using an improved atmospheric GCM (AGCM), Krinner et al. (2012) further suggested that the open-water surface effect was underestimated in previous studies that reported the northward WAM shift, with a consequence of a doubling of the regional precipitation rates. However, the disadvantage of LK_98 is that it does not include any other MH Megalakes beyond Megalake Chad (Holmes & Hoelzmann, 2017). Hence, Chandan and Peltier (2020) further added dedicated MH Megalakes based on the small-lake map and investigated the lake effect using a fully coupled atmosphere-ocean GCM (AOGCM). They reported that the increase in precipitation from the lakes was weak, and the lake location did not considerably influence precipitation. Hence, the role of Megalake Chad in contributing to the humidification of the Sahara is still under discussion. Furthermore, the lakes in the

删除了: the
删除了: Desert
删除了: (Claussen, M. et al., 2017)
删除了: feedback
删除了: feedback
删除了: MH_98
删除了: as
删除了: MH_98
删除了: to

western Sahara also potentially contribute to WAM. Tegen et al. (2002) further indicated the presence of larger lakes and wetlands over the western Sahara based on dust emission simulations (hereinafter potential maximum-lake map; LK_02 in Tables 1 and S1). Based on the LK_98 and LK_02 lake maps, Specht et al. (2022) investigated the impacts of the latitudinal position of lakes and wetlands on changes in precipitation and initially highlighted the influence of western lakes on the northward WAM shift. These studies suggested that western lakes and Megalake Chad may play different roles in humidifying the Sahara, and this aspect requires further investigation.

The above-mentioned studies on lake-climate impact also explored the underlying physical mechanisms by which lake thermal and dynamic forcing affects the atmospheric circulation of the African monsoon system. For example, compared with the enhanced localized water cycling forced by lake evaporation (Broström et al., 1998; Carrington et al., 2001), Krinner et al. (2012) considered that the cooling effect that stabilizes convection is only locally applicable to deep lakes but increases the predictable water in summer and delays cooling in autumn, thereby extending monsoon. Recent studies have explored the mechanisms of how various components of the NAf monsoon system, including the Sahara Heat Low (SHL) and Sahara Highs in western Sahara, the African Easterly Jet (AEJ) in the middle atmosphere (600 hPa), and Tropical Easterly Jet (TEJ) in the upper atmosphere (200 hPa) influence the near-surface westerly flow northward and rainfall (Biasutti & Sobel, 2009; Claussen et al., 2017; Kuete et al., 2022). However, discrepancies exist regarding the effects of these components. Chandan and Peltier (2020) suggested that such a cooling effect could weaken the SHL and local convection, reducing the precipitation. Conversely, Specht et al. (2022) found that a weakened AEJ enhanced inland moisture transportation, leading to a northward and prolonged rain belt. As a result, the mechanisms of lake-climate interaction in the NAf monsoon system remain unclear.

To address these issues, the present study assessed the contribution of Western Sahara lakes and Megalake Chad in humidifying the Sahara region during the MH using the isotope-enabled AGCM MIROC5-iso (Okazaki & Yoshimura, 2019). To consider the large uncertainty in MH lake reconstructions (Quade et al., 2018), sensitivity experiments have been conducted with the original two sets of lake reconstructions (Hoelzmann et al., 1998; Tegen et al., 2002) and the recently-updated high-resolution lake and wetland reconstructions maps (Chen et al., 2021) over the NAf during the MH. We discuss the influence of Western Sahara lakes and Megalake Chad on the WAM movement and the potential lake-climate mechanisms involved to sustain the Green Sahara.

2 Materials and Methods

2.1 Experiments and settings

We used the isotope-enabled version of the Model for Interdisciplinary Research on Climate version 5 (MIROC5, Watanabe et al., 2010), called hereafter MIROC5-iso (Okazaki and Yoshimura, 2019). MIROC5-iso adopts a three-dimensional primitive equation in the hybrid σ–p coordinate system. The resolution of MIROC5-iso was set to a horizontal spectral truncation of T42 (~280 km) and 40 vertical layers with coordinates. The parameterization schemes have been

删除了: MH_02
删除了: MH_98
删除了: MH_02
删除了: ,
删除了: feedback
删除了: Using the latest information on
删除了: the contribution of
删除了: on
删除了: has been further discussed
删除了: further stressed
删除了: On the contrary
删除了: Owing to these discrepancies

comprehensively described by Watanabe et al. (2010), Okazaki and Yoshimura (2019), and Kino et al. (2021). The MIROC land component is the Minimal Advanced Treatments of Surface Interaction and Runoff (MATSIRO) model (Takata et al. 2003), which could simulate important water and energy circulation. The lake module simulates the thermal and hydrological processes of lakes and their interaction with the atmosphere. It should be noted that a minimum lake depth threshold (10 m) is set, which means the lake permanently existed. Such isotope-enabled climate models have proven to be valuable tools for tracing water vapor transportation and identifying the sources of precipitation changes (Tharammal, T. et al., 2021; Liu, X. et al., 2022).

To assess the hydroclimatic influence of the presence of lakes in NAf (0°–35° N; 20° W–40° E), we performed two control simulations for the pre-industrial (year 1850, PI_{ref}) and MH (MH_{ref}) period and six MH sensitivity experiments (see Table 1). For every experiment, orbital forcing and greenhouse gas concentrations were set according to the PMIP4 protocol (Otto-Bliesner et al., 2017). Land surface boundary conditions (such as land-sea mask, ice sheets, soils, vegetation, and lakes) were set according to the Coupled Model Intercomparison Project Phase 5 (CMIP5) protocol for MIROC5 (Watanabe et al., 2010). It should be noticed that the lake fraction is treated as the prescribed boundary conditions in the model based on the corresponding datasets, as the model cannot simulate the lake dynamically. Specifically, the Earth Topography five-minute grid (ETOPO5, https://www.ngdc.noaa.gov/mgg/global/etopo5.HTML) was used as global lake map boundary conditions for the control simulations. In MH_{ref} and PI_{ref} experiments, the presence of lakes in North Africa (NAf) is minimal, using the global lake fraction map from the ETOPO5 as in MIROC5 standard simulations (Figure S1). In contrast, the other experiments show highly varied lake fractions, indicating a much higher lake fraction in those cases. Meanwhile, The distribution of vegetation types for all experiments can be observed in Figure S2. It is evident from the map that NAf is predominantly characterized by bare ground coverage. Each experiment was run for 60 years, and only the last 30 years were used for our analyses to get the soil moisture (SM) of the study at an equilibrium state, indicating a balanced land surface water budget. We used sea surface temperature, sea ice concentration, and water isotope content of the sea surface provided by MPI-ESM-wiso (Cauquoin et al., 2019) as boundary conditions for our PI and MH simulations. In our six sensitivity MH experiments, only the lake map was changed in NAf, while other boundary conditions were kept the same as in MH_{ref} (Table 1).

Table 1. Experiments Setting

Experiment	GHG + Orb	Sea Surface	Lakes in the North Africa
PI_{ref}	PI*1	PI*2	ETOPO5*3
MH_{ref}	MH*1	MH*2	ETOPO5*3
MH_{C}			LK_98*4
MH_{WC}			LK_02*4
MH_{WCE1}			LK1*4

删除了: changes in

删除了: as reference

删除了: PI and MH simulations

删除了: MIROC5-iso

删除了: Figure S1a shows the global lake distribution used for MH_{ref} and PI_{ref} experiments using ETOPO5 as in MIROC5 standard simulations. We found that few lakes existed in NAf (Figure S1b). ...

删除了: MH

删除了: MH

删除了: MH

MH$_{WCE2}$	LK2*4
MH$_{WCE3}$	LK3*4
MH$_{WCE4}$	LK4*4

*1 Following PMIP4 Protocol

*2 Cauquoin, Werner et al. (2019)

*3 National Geophysical Data Center, 1993. 5-minute Gridded Global Relief Data (ETOPO5) National Geophysical Data Center, NOAA. Doi:10.7289/V5D798BF.

*4 The details of the lake reconstructions can be seen in Table S1.

The reconstructed lake maps in NAf used for our sensitivity experiments are summarized in Table S1 and are shown in Figure 1. MH$_C$ uses the LK_98 lake map (Hoeltzmann et al., 1998), with only Megalake Chad, over 15°–20° E and 10°–20° N (Figure 1a). The MH$_{WC}$ experiment uses the LK_02 lake maps (Tegen et al., 2002) with more numerous western and northern lake areas over 0°–10° W and 10°–20° N in addition to Megalake Chad (Figure 1b). The MH$_{WCE1}$–MH$_{WCE4}$ experiments use the LK1-4 lake maps from Chen et al. (2021). They show an increasing lake fraction in Megalake Chad and eastern lakes in South Sudan around 0–20° N, with a gradually increasing scattered west lake area (Figure 1c–f) compared with the LK_98 and LK_02 lake maps. LK4 has the largest lake proportion in the western, eastern, and Megalake Chad regions, and differs from LK2 primarily in its representation of Megalake Chad (Figure 1d, 1f). The average main lake fraction over the NAf region according to these different reconstructions varies from 1-13 % compared to the total land areas of NAf (Figure 1g). It should be noticed that the water body delineated in LK_98 and LK_02 lake maps only pertain to the lake but the LK1-4 lake maps include both the wetland and lakes. Generally, lakes and wetlands are persistently saturated or near-saturated areas that are regularly subjected to inundation or shallow water tables in the absence of human disturbances (Tootchi et al., 2019). In this study, wetlands are also treated as lakes in our climate model.

删除了: MH

删除了: MH

删除了: MH

删除了: S2

删除了: MH_98

删除了: s

删除了: the

删除了: Figure S2

删除了: MH_02

删除了: Figure S2

删除了: MH1

删除了: Figure S2

删除了: MH_98

删除了: MH_02

删除了: MH4 accounting for the largest lake proportion among the western and eastern lakes, and the Megalake Chad, is mainly different from the MH2 lake map for the latter (Figure S2d and

删除了: 1-3

删除了: %

删除了: with

删除了: present

删除了: global land surface area (~1.48 × 108 km^2)

删除了: Figure S2

删除了: considered

删除了:

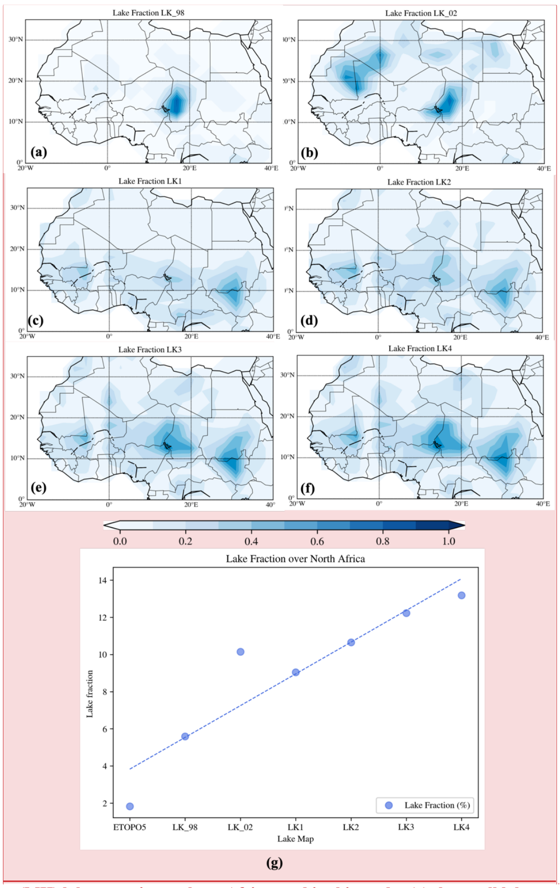

Figure 1: The mid-Holocene (MH) lake maps in northern Africa used in this study: (a) the small lake map derived by (Hoelzmann, Jolly et al., 1998) used for the MH_{C} experiments, (b) the maximum lake map derived by Tegen, Harrison et al. (2002) used for the MH_{WC} experiments, (c)-(f) the potential lake maps derived by Chen, Ciais et al. (2021) corresponding to four different types of precipitation, used for the MH_{WCE1}, MH_{WCE2}, MH_{WCE3} and MH_{WCE4} experiments, respectively. The lake maps differences mainly come from the western Sahara lakes, Megalake Chad and eastern lakes in South Sudan (between 0°-20°N). (g) The fraction (circle size) of all the prescribed lakes experiments compared total land areas of North Africa (NAf, 0°–35° N; 20° W–40° E).

批注 [YL1]: Added from Supplementary Materials

We investigated the contribution of the Western Sahara lakes by comparing the MH_C and MH_{WC} experiments. The Megalake Chad's influence on NAf climate was assessed using the MH_{WCE2} and MH_{WCE4} results. For evaluation of our model results, we compared the isotope outputs from MIROC5-iso with available observations from natural archives (e.g., δ18O in ice cores and speleothems) as in Cauquoin et al. (2019).

删除了：quantified

2.2 Climate model validation method

To evaluate our MH simulation, we used measured isotope datasets from ice cores and continental speleothems. We used 5 Greenland and 10 Antarctic ice cores, selected from the comprehensive compilations of Sundqvist, Kaufman et al. (2014), and WAIS Divide Project Members (Fudge, Steig et al., 2013). These are presented in Table 1 of Cauquoin et al. (2019). We also added to this dataset MH−PI δ18O anomalies measured from four (sub)tropical ice cores (Huascaran, Sajama, Illimani, and Guliaa ice cores), which are reported by Risi et al. (2010). Furthermore, we extracted 57 entities from the SISALv2 (Speleothem Isotope Synthesis and Analysis version 2) dataset (Comas-Bru et al., 2020 ESSD), for which averaged δ18O values of calcite or aragonite are available for both the MH and PI period. As recommended by Comas-Bru et al. (2019), we defined here PI and MH as the means of 1850-1990 CE and 6 ± 0.5 ka periods, respectively. The measured δ18O of calcite or aragonite are converted into δ18O of drip water using equations 1 or 2 of Comas-Bru et al. (2019), respectively, after conversion from V-PDB to V-SMOW scale (equation 3 of Comas-Bru et al. (2019)). The annual mean surface air temperature from MIROC5-iso is used for the conversion.

删除了：They

删除了：reported

删除了：in

删除了：Table 3 of

2.3 Analysis method

2.3.1 Hydroclimate analysis

We analyzed hydroclimate changes based on the ratio with the MH_{ref} results.

$$Ratio_{exp} = \frac{Exp - MH_{ref}}{MH_{ref}} \times 100\% \,, \quad (1)$$

The water vapor flux was also calculated to explain the precipitation changes. The zonal component of the vertically integrated flux (Fu) is:

$$F_u = \int_{300hpa}^{ps} \frac{uq}{g} dP \,, \quad (2)$$

where u is the zonal wind, q is the specific humidity, p is the pressure at a given vertical level, g is the gravitational acceleration (9.8 m/s), and ps is the surface pressure. The meridional component of the vertically integrated flux (Fv) is expressed as:

删除了：horizontal

$$F_v = \int_{300hpa}^{ps} \frac{vq}{g} dP \quad (3)$$

By combining Fu and Fv, the integrated vapor transport can be expressed as:

$$IVT = \sqrt{F_u^2 + F_v^2} \quad (4)$$

2.3.2 Budyko's aridity index

To assess climate zone transformation with the balance between available energy (net surface radiation) and water (precipitation) at the surface, Budyko's aridity index (Budyko & Miller, 1974) was calculated as a joint analysis using hydro-climatological variables as follows:

$$I = \frac{R_n}{lP} \quad (5)$$

where R_n is the net surface radiation, l is the latent heat coefficient (2.5×10^6 J/kg), and P is the precipitation at the surface. The change in the aridity index indicates regional shifts in hydroclimatic conditions.

The annual mean of net radiation and precipitation were used in the analysis. A higher Budyko aridity index indicates a drier region due to the available energy being high relative to the amount of water, whereas a lower index indicates a more humid region due to the available energy being low relative to the amount of water. In our study region, six climate regions are classified by Budyko aridity index: Tropical Humid ($I \leqslant 0.7$), Humid ($0.7 < I \leqslant 1.2$), Semi-Humid ($1.2 < I \leqslant 2.0$), Semi-Arid ($2.0 < I \leqslant 4.0$), Arid ($4.0 < I \leqslant 6.0$) and Hyper-Arid ($6.0 < I$). The equation suggests that changes in the dryness index within a region are more indicative of shifts in the hydroclimatic regime over the long term rather than intra-annual variability, such as individual drought events.

3 Results

3.1 Model reproducibility

To evaluate the MH_{ref} results at the global scale, we compared MH_{ref} - PI_{ref} with isotopic observations (Figure S3). We found a good model-data agreement, with a root mean square error and R-squared values of 0.81 ‰ and 0.33, respectively. Also, MIROC5-iso simulates a decrease in the isotopic composition of precipitation over NAf due to the enhanced monsoon during MH, in agreement with previous model studies (Schmidt et al., 2007; Risi et al., 2010; Cauquoin et al., 2019). Our simulation bias mainly originated from the ice cores in Antarctica and the speleothems in North America (Figure S3a). The isotopic performances in the PI_{ref} simulation were verified in Okazaki and Yoshimura (2019) and Kino et al. (2021). Other previous studies also confirmed the general reproducibility of global MH characteristics using the MIROC-series (O'Ishi & Abe-Ouchi, 2011; Ohgaito et al., 2021).

删除了: based on

删除了: experiments

To further examine the model performance in North Africa, we compare our precipitation result with Figure 4a in the study conducted by Larrasoaña et al. (2013). From Figure S4a, our results indicate that the MIROC5-iso was hard to reproduce the northward shift of the zone with precipitation less than 1000mm/year, but show good agreement with the reconstructed map in the zone with precipitation exceeding 1000mm/year. Besides, we also compared our result with precipitation and summer season temperature anomalies between 6ka-0ka, as provided by Bartlein et al. (2010) (Figure S4b-e). This comparison also revealed precipitation underestimation in the northern NAf and lower temperatures in the central NAf. These comparisons collectively suggest a simulation bias of the MIROC5-iso model in North Africa, particularly concerning the northward movement of the monsoon system.

We also examined the model representation of WAM characteristics (Claussen et al., 2017). Based on the annual cycle of WAM (Thorncroft et al., 2011), we defined summer as June-July-August-September (JJAS) and winter as January-February-March (JFM). We focused on summer because of the large amount of precipitation caused by WAM. In both MH_{ref} and PI_{ref}, the Sahara Highs in the middle atmosphere were positioned at 20°–30° N and centered at 0° E (contours in Figures 2a and 2d). In the middle atmosphere, AEJ was found at 10°–15° N, corresponding to the precipitation belts (vectors and shaded areas in Figures 2a and 2d), and the concurrent TEJ at 0°–10° N in the upper atmosphere (vectors in Figures 2b and 2e). In the lower atmosphere (850 hPa), the SHL, centered in the hottest Sahara region at 10°–20° N (contours in Figures 2c and 2f), was associated with the monsoon westerly winds from the equatorial Atlantic Ocean to the continent (vectors in Figures 2c and 2f). While the monsoon westerly flow was at ~10° N in PI_{ref}, it moved to ~15° N in MH_{ref}. Given that the model bias and uncertainty in reproducing the AEJ still require improvement in reanalysis datasets (Kuete et al., 2022), our climate model efficiently captured the WAM patterns for investigating the sensitivity of WAM to lake expansions in the Sahara.

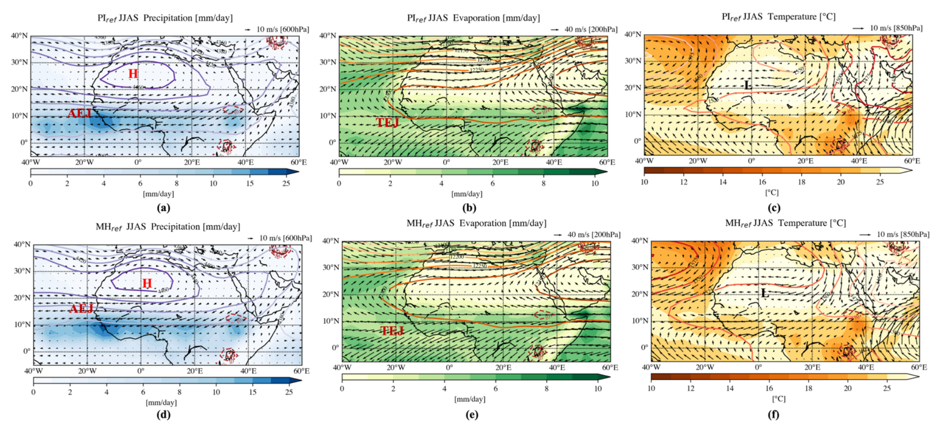

Figure 2: The simulated climatological precipitation and temperature responses for the Pre-industrial (PI) and mid-Holocene (MH) reference experiments on the summer season (June-July-August-September, JJAS). For PI experiment: Subplot (a) is the precipitation with 600h Pa wind (arrow) geopotential high (counters). Subplot (b) is the evaporation with 200h Pa wind (arrow) and geopotential high (counters). Subplot (c) is the surface temperature with 850h Pa wind (arrow) and geopotential high (counters). Subplots (d), (e) and (f) are the same as (a), (b) and (c), respectively, but for MH experiment. For (a-f), lake fraction [%] contours of the respective lake sensitivity experiment are shown with the red dashed lines, and the respective reference scale for the arrow is shown at the right top of each panel. The corresponding high pressure system, low pressure system, Africa Easterly Jet and Tropical Easterly Jet have been marked with 'H', 'L', 'AEJ' and 'TEJ'.

删除了: further
删除了: Figures 1
删除了: 1
删除了: Figures 1
删除了: 1
删除了: Figures 1
删除了: c
删除了: 1
删除了: f
删除了: Figures 1
删除了: b
删除了: 1
删除了: e
删除了: Figures 1
删除了: b
删除了: 1
删除了: e
批注 [YL2]: Corrected the Season Mean Calculation
删除了: 1
删除了: surface temperature
删除了: 850h
删除了: c
删除了: d
删除了: b
删除了: PI
删除了: c

3.2 Hydroclimatic responses to the lakes in NAf

We investigated the influence of lake distribution in NAf on the hydroclimatic response by analyzing the differences between our lake sensitivity simulations and MH_{ref} for summer. First, we examined the influence of the Western Sahara lakes presence in addition to Megalake Chad. Without the Western Sahara lakes (MH_{C}), Megalake Chad marginally changed local precipitation and water transportation (shaded areas and vectors in Figure 3a). However, owing to the western lakes (MH_{WC}), the precipitation belt (originally at ~10° N in Figures 3a) strengthened, expanding northward and eastward to Megalake Chad (shaded areas in Figure 3b), and was associated with the enhanced anticlockwise water vapor transportation (vectors in Figure 3b). These findings suggested that the Western Sahara lakes enhanced the northward WAM extension. We further compared MH_{WCE2} and MH_{WCE4} experiments (Figures 3c and 3d) to MH_{ref} in order to assess the impact of Megalake Chad size on the hydroclimatic influence of western lakes. We found that the western lakes at 10°–20° N could induce an enhanced precipitation belt with northwestward water transportation in the MH*WCE2* experiments (Figure 3c). With the expansion of Megalake Chad and eastern lakes, the precipitation belt extended eastward with a strengthened positive response (Figure 3d), suggesting the influence of Megalake Chad in eastward monsoon extension.

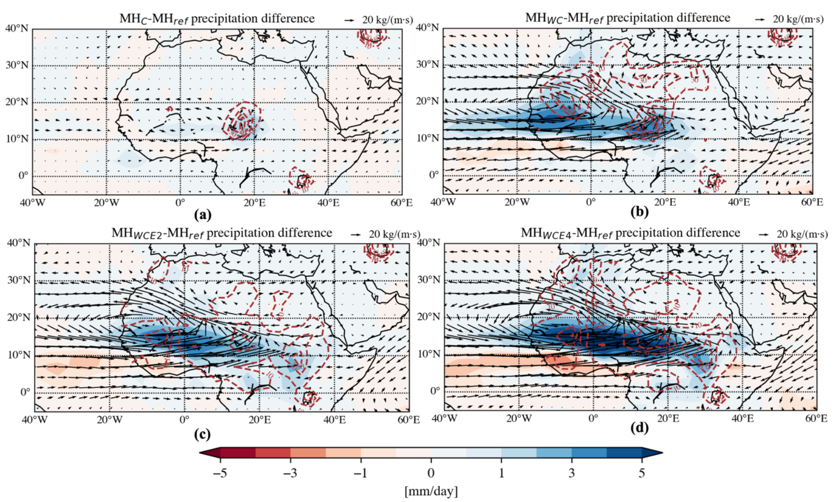

Figure 3: Anomalies relative to MH_{ref} in simulated mid-Holocene climatological summer mean (June-July-August-September, JJAS) precipitation (shades) and integrated vapor transportation (IVT; arrows) for (a) MH_{C}, (b) MH_{WC} and (c) MH_{WCE2} and MH_{WCE4} experiments, respectively. For (a)-(d), the lake fraction [%] contours of the respective lake sensitivity experiment are shown with the red dashed lines (contour spacing: 10%-30%-50%-70%-100%), and the respective reference scale for the arrow is shown at the right top of each panel.

删除了: 2
删除了: Figures 1
删除了: and 1d
删除了: 2
删除了: 2
删除了: 2
删除了: 2
删除了: 2
删除了: 2
批注 [YL3]: Corrected the Season Mean Calculation
删除了: **2**

Further, to investigate the mechanisms of the monsoon response to lake expansions, we analyzed the responses in land surface climate variables (soil moisture (SM), evaporation (Evap), and surface temperature (T2); shaded areas in Figure 4) and atmospheric circulations (geopotential height and horizontal winds; contours and vectors in Figure 4). In MH_{C}, Megalake Chad did not affect atmospheric circulations, but it affected the local hydrological cycle with slight increases in SM and Evap by 0.2 m and 2 mm/day, resulting in surface cooling around Megalake Chad by -0.4°C (Figure 4a, 4b, and 4c). In MH_{WC}, the western lakes induced similar local responses around the western lakes, with increased SM and evaporation flux accompanied by a surface cooling in northwest NAf, but with a stronger response than around Megalake Chad (Figure 4d, 4e, and 4f). The expansion of the western lakes impacts the atmospheric circulation, too. In the upper troposphere (200 hPa), TEJ was enhanced at 5°–15° N (vectors in Figure 4d). Further, the anticlockwise anomalies of horizontal winds in the middle atmosphere (vectors in Figure 4e), associated with the weakened Sahara High (contours in Figure 4e), suggested that the AEJ was weakened and shifted northward. In the lower atmosphere, the enhanced monsoon westerly flow at ~10°–20° N (vectors in Figure 4f) was associated with cyclone circulation over the Atlantic Ocean at ~20°–30° N, next to the weakened SHL (contours in Figure 4f).

Similar responses on hydroclimatic variables and atmospheric circulation were also found in MH_{WCE2} and MH_{WCE4} as in MH_{WC}. The increases in SM, Evap, and T2 extended more eastward in MH_{WCE4} (Figure 4j, 4k, and 4l) compared with those in MH_{WCE2} (shaded areas in Figure 4g, 4h, and 4i). The associated atmospheric circulation was further enhanced and extended eastward. Specifically, the TEJ became stronger, and Sahara High further weakened with stronger anticyclonic circulation anomalies extending eastward, leading to a weaker AEJ in MH_{WCE4} than in MH_{WCE2} (contours and vectors in Figure 4g, 4j 4h, and 4k). Moreover, the above cyclonic circulation in the lower atmosphere shifted southeastward at ~20° W, further extending the monsoon westerly flow eastward in MH_{WCE4} compared with that in MH_{WCE2} (contours and vectors in Figure 4i and 4l). Notably, owing to the southeastward extension of the cyclonic circulation response, the weak SHL signals in the MH_{WCE4} experiments were counterbalanced and became weakened compared to those in both MH_{WC} and MH_{WCE2} experiments (contours in Figure 4f, 4i, and 4l).

Hence, the enhanced northward WAM forced by lakes can be explained by lake expansions that induce a cyclonic circulation in the lower atmosphere, accompanied by a weakened AEJ and stronger TEJ associated with weakened Sahara Highs and SHL. Similar mechanisms have been previously identified based on observations and simulations, although their physical mechanisms are still under discussion (Nicholson, 2009; Lavaysse et al., 2010; Klein et al., 2015; Nicholson & Klotter, 2020). Furthermore, we found that the lake-induced precipitation and SM increment were close to those induced by orbital forcing only, but restricted over ~10° N (Figure S5a and S5b). It confirms that lake expansion considerably affected the humidification of NAf. In summary, Western Sahara lake and Megalake Chad could enhance northward WAM triggered by orbital forcings, resulting in a significant humidifying effect.

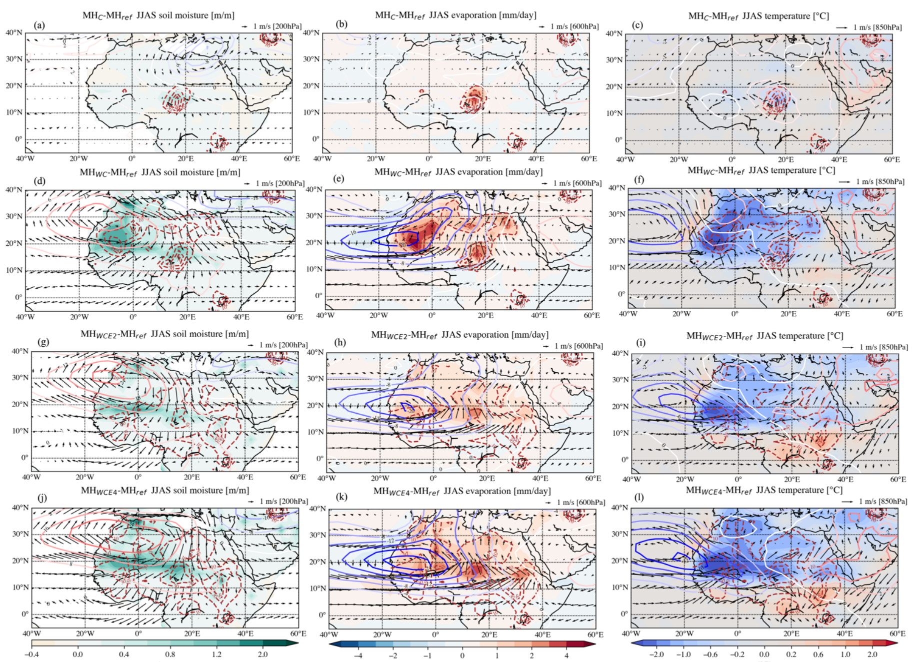

Figure 4: Simulated mid-Holocene climatological JJAS mean anomalies with respect to MH$_{ref}$: (a) soil moisture (shades) with 200 hPa wind (arrows) and geopotential height (contours), (b) evaporation (shades) with 600 hPa horizontal wind (arrows) and geopotential height (contours) and (c) surface temperature (shades) with 850 hPa horizontal wind (arrows), and geopotential height (contours) for MH$_C$ experiment. Map (d), (g), and (f) are the same as (a), (b) and (c), respectively, but for the MH$_{WC}$ experiment. Maps (g), (h) and (i) are the same as (a), (b), and (c), respectively, but for the MH$_{WCE2}$ experiment. Maps (j), (k), and (l) are the same as (a), (b) and (c), respectively, but for the MH$_{WCE4}$ experiments. For all the maps, the lake fraction [%] contours of the respective lake sensitivity experiment are shown with the red dashed lines, and the respective reference scale for the arrow is shown at the right top of each panel.

3.3 Aridity transformation with lake expansions

To understand the influence of Western Sahara lakes and Megalake Chad on the hydroclimatic spatial response, we further calculated the anomaly changes of regionally averaged hydroclimate variables with lake expansion over NAf (Figure 4). Considering PI$_{ref}$ experiments as the reference, the annual mean variables exhibit linear relationships with the mean lake fraction over NAf. The annual mean values of Precipitation (Prcp), Evap, and Net Radiation (Rad) increase with lake fraction, whereas T2 decreases (crosses in Figure 5). To provide further insights into the changes in radiation (Rad), we examined the relationship between net longwave radiation (LW) and net shortwave radiation (SW) in relation to the lake

批注 [YL4]: Corrected the Season Mean Calculation; Corrected the Soil Moisture Unit

删除了: 3

删除了: zonally

删除了: 4

fraction (Figure S6a), positive downward). Take MH_{WCE4} experiments as an example, our analysis revealed that the increase in Rad can be attributed to two factors: the increase in downward LW in the cooling and humidifying areas (Figure S6b) and the slight increase in downward SW in the regions with higher lake fraction, which is associated with changes in surface albedo (Figure S6c). These findings suggest that the humidifying and cooling areas experienced greater incoming LW radiation absorption.

Additionally, seasonal analysis shows that during summer, there are considerable differences between the lake sensitivity experiments and the PI_{ref}, with positive anomaly offsets for Prcp, Evap, and Rad and negative anomaly offsets for T2 (upward triangles in Figure 5). Whereas, during winter, these variables are not significantly related to the lake expansion (standard deviation = ~0.1), but a cooling effect is still observed (downward green triangles in Figure 5). Therefore, the lake expansion mainly affects hydrological changes in summer, leading to wetter and cooler conditions in the lake sensitivity experiments compared to the MH_{ref}. However, the unusually high anomalies observed during summer in the MH_{WC} experiments suggest that the position of the lake may play a more important role than the proportion of lakes in moistening the Sahara regions.

删除了: However, the unusually higher anomalies in the MH_{WC} experiments suggested that the importance of the lake position potentially outweighs the proportion of lakes. Specifically, the statistical analysis results for summer indicate considerable offsets in the MH_{WC} results (positive anomaly offsets for Prcp, Evap, and Rad and negative anomaly offsets for T2; upward triangles in Figure 4), whereas for winter, these variables were not related with the lake expansion (standard deviation = ~0.1), but a cooling effect still existed (downward green triangles in Figure 4). Additionally, lake expansion mainly contributes to the hydrological changes in summer, that is, wetter and cooler conditions are simulated in summer in the lake sensitivity experiments than in the MH_{ref} one. …

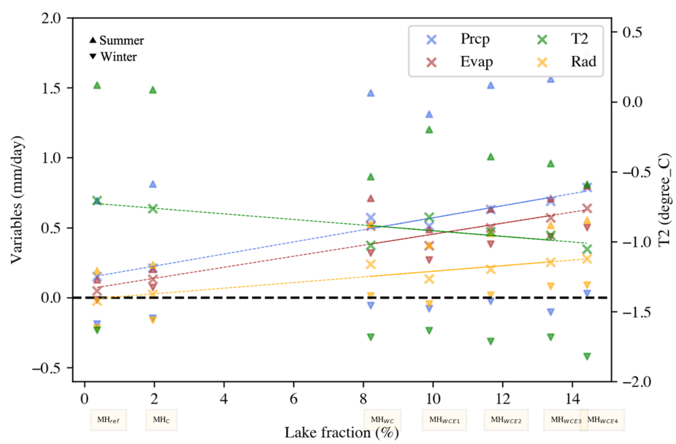

Figure 5: Statistical relationship between regionally averaged hydroclimate variables anomaly and averaged grid lake fraction over Northern Africa (20°W–40°E, 0–35°N) for MH lake experiments anomalies (relative to PI_{ref}) on the annual (cross), JJAS (upward triangle) and JAM (downward triangle) averages. The hydroclimatic variables include precipitation (Prcp [mm/day]; blue), evaporation (Evap [mm/day]; brown), 2 m air temperature (T2 [°C]; green), and radiation (Rad [mm/day], downward as positive; yellow). The p-value is less than 0.05 for all the relationships.

批注 [YL5]: Corrected the Season Mean Calculation

删除了: 4

删除了: zonally

We used here the Budyko aridity index to detect changes in hydroclimatic conditions related to lake expansion. Compared with the MH_{ref} experiments (Figure S7a), the northwest climate zones are transferred from hyper-arid to arid and semi-arid zones due to the lake expansions in our six MH sensitivity experiments. Moreover, the western arid and semi-arid zone areas

删除了: 5

are reduced with increasing northward humid and semi-humid zones, along with increasing tropical humid zones (Figure S8). Additionally, in the MH_{WCE4} experiments, such climate zones extend further eastward, corresponding to the spatial response of hydroclimatic variables. Correspondingly, the mean Budyko aridity index anomaly over NAf relative to PI_{ref} increases with lake expansion, indicating that the aridity extent is lower with the presence of lakes (dots in Figure 6a). Climate zone transformation indicates the essential role of lake-climate impact in sustaining the northwest humidification of the Sahara by changing the hydroclimatic conditions and alleviating aridity.

However, our climate zone results show that there are still hyper-arid and arid zones over the northwestern Sahara. Hence, we further demarcated regions of the precipitation scarcity and surplus based on the threshold of semi-humid climate zones (I = 2). By comparing the simulated precipitation with the semi-humid climate zone threshold, the regions receiving less than the threshold are considered as scarce, and regions receiving more are considered as surplus. The total amount of precipitation scarcity was ~140–160 mm/d, and the precipitation surplus was ~260–370 mm/d over NAf and continued to increase with lake expansion (bars in Figure 6a). Compared with the MH_{ref} results, the MH_{WCE4} experiments potentially reduced precipitation scarcity by up to ~13% and increased precipitation surplus by ~40%. The spatial patterns showed that the north-dry and south-wet precipitation pattern (Figures S7b and S9) and the dividing line moved up to ~5° to the north compared with the MH_C experiments over the western NAf regions (Figure 6b). Additionally, precipitation scarcity values were lower in the western region and higher in the eastern region.

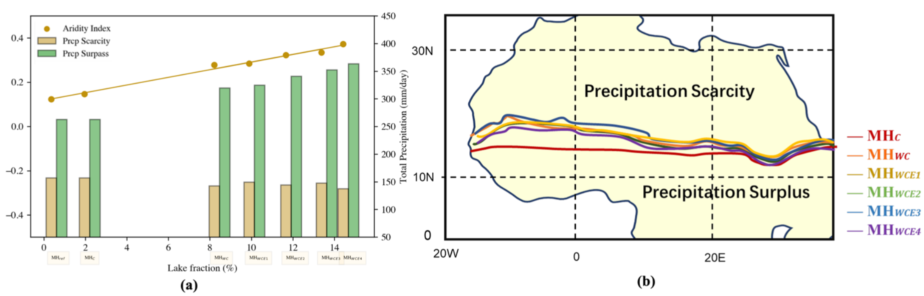

Figure 6: (a) Budyko Aridity index anomaly between PI_{ref} and MH simulations (left y-axis; unitless) with different averaged grid lake fractions as well as the total precipitation scarcity amount (brown bar; mm/day) and total precipitation surplus amount (green bar; mm/day) corresponding to the right y-axis. All the variables are climatological mean annual values. (b) The border between regions of precipitation scarcity zones and precipitation surplus zones for all the mid-Holocene experiments.

Notably, such north-south inverse patterns were also observed in the spatial responses of SM (Figures 4g and 4j), Evap (Figures 4h and 4k), and T2 (Figures 4i and 4l). Specifically, SM and Evap showed positive anomalies with a cooling effect in the north of 10° N, and minor or negative anomalies but with a warming effect in the south of 10° N over NAf. However, such near-equatorial (around 0°–10° N) warming effect cannot be explained solely by the reduced precipitation in MH_{WCE2} and MH_{WCE4} as the enhanced precipitation belt covered the entire tropical area (0°–20° N), in contrast to being concentrated

删除了: 6
删除了: Figure 5
删除了: feedback
删除了: estimated
删除了: ≤
删除了: , implying that the climate zones over NAf were at least semi-humid or wetter.
删除了: 7
删除了: 8
删除了: Figure 5
删除了: modes
删除了: 5
删除了: 7
删除了: Figure 5
删除了: precipitation scarcity was less in the west and more in the east.
批注 [YL6]: Corrected the Fig 6a label
删除了: 5
删除了: boarding line
删除了: Figure
删除了: 3
删除了: 3
删除了: 3
删除了: 3
删除了: 3
删除了: 3
删除了: in MH_{WCE2} and MH_{WCE}
删除了: and not just

in the WAM regions (around 10°–20° N) in MH_{WC}. To identify the inverse temperature anomalies pattern in MH_{WCE2} and MH_{WCE4}, we analysed the stable oxygen isotope ratio ($\delta^{18}O$) in precipitation (Figure S10). Positive $\delta^{18}O$ anomalies suggested the presence of an oceanic moisture source in addition to the local lakes, whereas negative anomalies indicated the influence of local water cycling. The $\delta^{18}O$ increase in the northern regions suggests the moisture sources from the Atlantic Ocean are associated with westerly monsoon winds. Conversely, the equatorial land areas show decreases in $\delta^{18}O$, which are also current with weakened evaporation (Figure 4k) and warming effects (Figure 4l). Further examination of the $\delta^{18}O$ decrease (Figure S10d) in the equatorial land areas suggested that the slight precipitation increment (Figure 4d) was not driven by the westerly monsoon winds. Instead, such a warming effect induced by equatorial lakes may link to the differences in lake heating during daytime and night (Thiery et al., 2015). Hence, while lakes in WAM regions tend to result in wetter and cooler climatic responses, lakes located elsewhere (such as the eastern lakes in South Sudan) may not impact the northward WAM movement.

4 Discussion and Conclusions

We used the MIROC5-iso model with different GS lake maps to investigate the influence of Western Sahara lakes and Megalake Chad on the northward movement and eastward expansion of WAM, leading to the humidity in the Sahara region. Our results showed that Western Sahara lakes promote the northward movement of WAM, and Megalake Chad can further enhance the monsoon westerly flow response eastward. This cyclonic response in the lower atmosphere, is associated with weakened AEJ, SHL, Sahara Highs, and strengthened TEJ (Figure 7). Additionally, the humidifying transformation of the climate zone and the reduction in precipitation scarcity over NAf further highlight the important influence of lake expansion in reconstructing the GS climate.

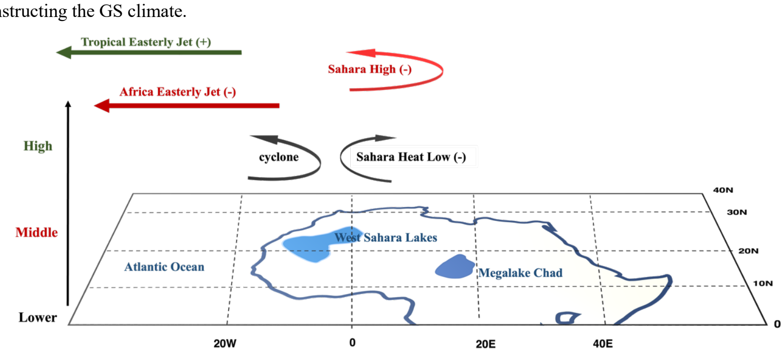

Figure 7: Lake-climate impact mechanism over North Africa in the mid-Holocene. The lower, middle, and high atmosphere circulation are marked with black, red, and green colors, respectively. The weakening signal is represented by '-', and the strengthening signal is represented by '+'.

删除了: as observed
删除了: 8
删除了: , which suggested
删除了: ,
删除了: decrease in
删除了: 8
删除了: with weakened evaporation (Figure 3k) and warming effects (Figure 3l) …
删除了: irrelevant t
删除了: o
删除了: S
删除了: n inverse
删除了: be related to the special equatorial location with
删除了: differences
删除了: lakes in WAM regions exert wetter and cooler climatic responses. Contrastingly, if lakes are not located in WAM regions, lakes do not affect the northward WAM movement, like the eastern lakes in South Sudan.
删除了: Based on the MIROC5-iso model simulation results using different GS lake maps, we discussed the roles of Western Sahara lakes and Megalake Chad positively influencing the northward movement and eastward expansion of WAM humidifying the Sahara region. Our results showed that Western Sahara lakes promote the
删除了: 6
删除了: **6**
删除了: **feedback**

Our study confirmed that Megalake Chad does not influence the northward monsoon movement when western lakes are missing (Broström et al., 1998; Carrington et al., 2001; Chandan & Peltier, 2020). We also confirmed the influence of Western Sahara lakes on the northward monsoon movement (Specht et al., 2022), but further stressed that Megalake Chad could extend the westerly monsoon eastward when accompanied by Western Sahara lakes. Besides, compared with our simulations (Figure S11), Chandan and Peltier (2020) underestimated the contribution of lakes, approximately close to MH_{WC} results, by supposing that the weakened SHL induced by the surface cooling effect would reduce precipitation. However, we found that such an SHL weakening effect can be offset by the adjacent cyclonic circulation response in the lower atmosphere, which promotes precipitation. Moreover, we found that the northward WAM movement goes with a weakened AEJ and a strengthened TEJ, in agreement with Specht et al. (2022). Therefore, we emphasized the importance of how the climate model represents the AEJ and TEJ behaviors in reproducing the MH climate (Claussen et al., 2017; Bercos-Hickey et al., 2020; Ngoungue et al., 2021). Furthermore, regarding the lake position (Chandan & Peltier, 2020; Specht et al., 2022), we suggest that both the western lakes and Megalake Chad located in the WAM regions may have played a crucial role in inducing the monsoon movement. Finally, the influence of Sahara lakes on climatic zone transformation in NAf is important, as corroborated by the Budyko aridity index. Such lake-climate response can humidify GS by transforming the climate zones from hyper-arid or arid to semi-arid or semi-humid, especially over the northwestern areas, and reduce the precipitation scarcity by up to 13%. However, our lake sensitivity experiments may not comprehensively capture the impact of small lake aggregates, which may limit the scope of our findings. Here we have included the precipitation and isotope anomalies (Figure S12), as well as the SM, Evap, and T2 with the low-mid-high level circulation responses (Figure S13) for MH_{WCE1} and MH_{WCE3}. The similarity of these results with MH_{WCE2} and MH_{WCE} confirms that the small lake aggregate effect is negligible in the large-scale lake-climate impact mechanisms. Nonetheless, conducting ideal sensitivity experiments in the future is necessary to confirm our findings and fully elucidate the impact of lakes on the regional hydroclimate during the mid-Holocene period.

Limited by the model integration and uncertainty, especially the lack of the dynamic lake or vegetation modules coupled with MIROC5-iso, the model-dependent findings of this study only focused on how the changes in the presence of lakes in terms of surface boundary conditions influence the GS hydroclimatic conditions without considering the climate reinforcement on lake expansion or shrinkage. Additionally, under the forcing of lake presence, the soil properties and vegetation growth changes also influence the water holding capacity, which determines the greening process. But these changes are limited by the simplified single-direction impact discussion. Furthermore, due to the absence of coupling with the ocean GCM, the model fails to consider the interactive effects of lake and SST or sea ice concentration, which are crucial to examine the teleconnection between the ocean and the WAM. Hence, dynamic model integration is required to provide new insights to understand single variable interactions and their joint effect on land-atmosphere interaction during the GS period (Dallmeyer et al., 2020). Moreover, understanding the external forcing, such as orbital parameters and greenhouse gas changes, which influence the GS climate system, would also provide insights into replicating the GS climate in the future (Duque-Villegas et al., 2022). Thus far, the interactive dynamic understanding among potential GS climate drivers is still

删除了: should be
删除了: to
删除了: induce
删除了: feedback
删除了: outer components
删除了: orbital forcing and greenhouses

unclear and different types of interactive feedback mechanisms contributing to the limitation of the uncertainty should be identified through climate proxy datasets.

In summary, our study identified lake expansions during the MH that sustain the Sahara greening with a northward movement and eastward extension of WAM. Limited by model dependency, particularly the inclusion or exclusion of certain feedback mechanisms such as dynamic lakes and vegetation modules, as well as the differences in model components and parameterizations used in different studies, the land-atmosphere interaction mechanism forced by dynamic lake changes remains unclear. Additionally, while the main features of the WAM have been adequately captured, higher-resolution simulations are required to simulate finer convective activities and provide new insights at the sub-grid scale (Steinig, S., et al. 2018; Ohgatio, R. et al., 2021). In the future, the dynamic lake module will be improved to detect the lake-climate interaction with time-varying lake extent in the simulations. Such research will reveal the dynamic interactive mechanism of lake-climate interactions and the possible conditions sustaining the Sahara greening processes.

删除了: and module integration

Code Availability

The code of the isotopic version MIROC5-iso is available upon request on the IIS's GitLab repository http://isotope.iis.u-tokyo.ac.jp:8000/gitlab/miroc-iso/miroc5-iso (Okazaki and Yoshimura, 2019).

Data Availability

The paleo small lake reconstruction maps (Hoelzmann, Jolly et al., 1998) and potential maximum lake reconstruction maps (Tegen, Harrison et al., 2002) used in this study for comparison are the processed ones published by Specht, Claussen et al. (2022), available at http://hdl.handle.net/21.11116/0000-0009-63B5-B. The updated 15 arc-second lake maps over the NA (Chen, Ciais et al., 2021) are available at Mendeley Data http://dx.doi.org/10.17632/8vfhhv8s2f.1 and we used the RFM2 model results in this study. Isotopic proxy datasets from ice cores used for the climate model validation method are reported in Table 1 Cauquoin et al. (2019). The SISALv2 dataset is available at https://doi.org/10.17864/1947.256 (Comas-Bru, Rehfeld et al. 2020).

Author contributions

KK and OT designed the research idea. YL and KK contributed to the experiment design. KK and AC provided model code and input data. YL performed the model experiments and results analysis. YL prepared the manuscript with contributions from all co-authors.

Competing interests.

The authors have no other competing interests to declare.

Acknowledgments

This work was supported by the Japan Society for the Promotion of Science [KAKENHI; 21H05002], the Environment Research and Technology Development Fund (JPMEERF20202005) of the Environmental Restoration and Conservation Agency of Japan, the Japan Society for the Promotion of Science via Grants-in-Aid 22K21323 and the advanced studies of climate change projection (SENTAN; JPMXD0722680395) from the Ministry of Education, Culture, Sports, Science and Technology (MEXT), Japan.

References

Bercos-Hickey, E., Nathan, T. R., & Chen, S.-H. (2020). On the Relationship between the African Easterly Jet, Saharan Mineral Dust Aerosols, and West African Precipitation. Journal of Climate, 33(9), 3533-3546. doi:10.1175/jcli-d-18-0661.1

Berger, A. (1988). Milankovitch Theory and climate. 26(4), 624-657. doi:https://doi.org/10.1029/RG026i004p00624

Biasutti, M., & Sobel, A. H. (2009). Delayed Sahel rainfall and global seasonal cycle in a warmer climate. Geophysical Research Letters, 36(23). doi:10.1029/2009gl041303

Braconnot, P., Albani, S., Balkanski, Y., Cozic, A., Kageyama, M., Sima, A., . . . Peterschmitt, J.-Y. (2021). Impact of dust in PMIP-CMIP6 mid-Holocene simulations with the IPSL model. Climate of the Past, 17(3), 1091-1117. doi:10.5194/cp-17-1091-2021

Braconnot, P., Otto-Bliesner, B., Harrison, S., Joussaume, S., Peterchmitt, J. Y., Abe-Ouchi, A., . . . Zhao, Y. (2007). Results of PMIP2 coupled simulations of the Mid-Holocene and Last Glacial Maximum – Part 1: experiments and large-scale features. Clim. Past, 3(2), 261-277. doi:10.5194/cp-3-261-2007

Brierley, C. M., Zhao, A., Harrison, S. P., Braconnot, P., Williams, C. J., Thornalley, D. J., ... & Abe-Ouchi, A. (2020). Large-scale features and evaluation of the PMIP4-CMIP6 midHolocene simulations. Climate of the Past, 16(5), 1847-1872.

Broström, A., Coe, M., Harrison, S. P., Gallimore, R., Kutzbach, J. E., Foley, J., . . . Behling, P. (1998). Land surface feedbacks and palaeomonsoons in northern Africa. Geophysical Research Letters, 25(19), 3615-3618. doi:10.1029/98gl02804

Budyko, M. I., & Miller, D. H. (1974). Climate and Life: Academic Press.

Carrington, D. P., Gallimore, R. G., & Kutzbach, J. E. (2001). Climate sensitivity to wetlands and wetland vegetation in mid-Holocene North Africa. Climate Dynamics, 17(2-3), 151-157. doi:https://doi.org/10.1007/s003820000099

Cauquoin, A., Werner, M., & Lohmann, G. (2019). Water isotopes – climate relationships for the mid-Holocene and preindustrial period simulated with an isotope-enabled version of MPI-ESM. Climate of the Past, 15(6), 1913-1937. doi:10.5194/cp-15-1913-2019

Chandan, D., & Peltier, W. R. (2020). African Humid Period Precipitation Sustained by Robust Vegetation, Soil, and Lake Feedbacks. Geophysical Research Letters, 47(21). doi:10.1029/2020gl088728

Cheddadi, R., Carre, M., Nourelbait, M., Francois, L., Rhoujjati, A., Manay, R., . . . Schefuss, E. (2021). Early Holocene greening of the Sahara requires Mediterranean winter rainfall. Proc Natl Acad Sci U S A, 118(23). doi:10.1073/pnas.2024898118

Chen, W., Ciais, P., Qiu, C., Ducharne, A., Zhu, D., Peng, S., . . . Huang, C. (2021). Wetlands of North Africa During the Mid-Holocene Were at Least Five Times the Area Today. Geophysical Research Letters, 48(20). doi:10.1029/2021gl094194

Chen, W., Ciais, P., Zhu, D., Ducharne, A., Viovy, N., Qiu, C., & Huang, C. (2020). Feedbacks of soil properties on vegetation during the Green Sahara period. Quaternary Science Reviews, 240. doi:10.1016/j.quascirev.2020.106389

Claussen, M., Dallmeyer, A., & Bader, J. (2017). Theory and Modeling of the African Humid Period and the Green Sahara. In: Oxford University Press.

Comas-Bru, L., Harrison, S. P., Werner, M., Rehfeld, K., Scroxton, N., Veiga-Pires, C., & members, S. w. g. (2019). Evaluating model outputs using integrated global speleothem records of climate change since the last glacial. Clim. Past, 15(4), 1557-1579. doi:10.5194/cp-15-1557-2019

Comas-Bru, L., et al. (2020). "SISALv2: a comprehensive speleothem isotope database with multiple age–depth models." Earth Syst. Sci. Data 12(4): 2579-2606.

Dallmeyer, A., Claussen, M., Lorenz, S. J., & Shanahan, T. (2020). The end of the African humid period as seen by a transient comprehensive Earth system model simulation of the last 8000 years. Climate of the Past, 16(1), 117-140. doi:10.5194/cp-16-117-2020

Duque-Villegas, M., Claussen, M., Brovkin, V., & Kleinen, T. (2022). Effects of orbital forcing, greenhouse gases and ice sheets on Saharan greening in past and future multi-millennia. Climate of the Past, 18(8), 1897-1914. doi:10.5194/cp-18-1897-2022

Fudge, T. J., Steig, E. J., Markle, B. R., Schoenemann, S. W., Ding, Q., Taylor, K. C., . . . Members, W. D. P. (2013). Onset of deglacial warming in West Antarctica driven by local orbital forcing. Nature, 500(7463), 440-444. doi:10.1038/nature12376

Harrison, S. P., Bartlein, P. J., Izumi, K., Li, G., Annan, J., Hargreaves, J., . . . Kageyama, M. (2015). Evaluation of CMIP5 palaeo-simulations to improve climate projections. Nature Climate Change, 5(8), 735-743. doi:10.1038/nclimate2649

Hoelzmann, P., Jolly, D., Harrison, S. P., Laarif, F., Bonnefille, R., & Pachur, H. J. (1998). Mid-Holocene land-surface conditions in northern Africa and the Arabian Peninsula: A data set for the analysis of biogeophysical feedbacks in the climate system. Global Biogeochemical Cycles, 12(1), 35-51. doi:10.1029/97gb02733

Holmes, J., & Hoelzmann, P. (2017). The late pleistocene-holocene African humid period as evident in lakes. In Oxford Research Encyclopedia of Climate Science.

Hopcroft, P. O., & Valdes, P. J. (2019). On the Role of Dust-Climate Feedbacks During the Mid-Holocene. Geophysical Research Letters, 46(3), 1612-1621. doi:10.1029/2018gl080483

Joly, M., and A. Voldoire, 2009: Influence of ENSO on the West African Monsoon: Temporal Aspects and Atmospheric Processes. J. Climate, 22, 3193–3210, https://doi.org/10.1175/2008JCLI2450.1.

Kino, K., Okazaki, A., Cauquoin, A., & Yoshimura, K. (2021). Contribution of the Southern Annular Mode to Variations in Water Isotopes of Daily Precipitation at Dome Fuji, East Antarctica. Journal of Geophysical Research: Atmospheres, 126(23). doi:10.1029/2021jd035397

Klein, C., Heinzeller, D., Bliefernicht, J., & Kunstmann, H. (2015). Variability of West African monsoon patterns generated by a WRF multi-physics ensemble. Climate Dynamics, 45(9-10), 2733-2755. doi:10.1007/s00382-015-2505-5

Krinner, G., Lézine, A. M., Braconnot, P., Sepulchre, P., Ramstein, G., Grenier, C., & Gouttevin, I. (2012). A reassessment of lake and wetland feedbacks on the North African Holocene climate. Geophysical Research Letters, 39(7). doi:https://doi.org/10.1029/2012GL050992

Kuete, G., Mba, W. P., James, R., Dyer, E., Annor, T., & Washington, R. (2022). How do coupled models represent the African Easterly Jets and their associated dynamics over Central Africa during the September–November rainy season? Climate Dynamics. doi:10.1007/s00382-022-06467-y

Kutzbach, J., Bonan, G., Foley, J., & Harrison, S. P. (1996). Vegetation and soil feedbacks on the response of the African monsoon to orbital forcing in the early to middle Holocene. Nature, 384(6610), 623-626. doi:10.1038/384623a0

Kutzbach, J. E., Guan, J., He, F., Cohen, A. S., Orland, I. J., & Chen, G. (2020). African climate response to orbital and glacial forcing in 140,000-y simulation with implications for early modern human environments. Proc Natl Acad Sci U S A, 117(5), 2255-2264. doi:10.1073/pnas.1917673117

Larrasoaña, J. C., Roberts, A. P., & Rohling, E. J. (2013). Dynamics of green Sahara periods and their role in hominin evolution. PloS one, 8(10), e76514.

Lavaysse, C., Flamant, C., & Janicot, S. (2010). Regional-scale convection patterns during strong and weak phases of the Saharan heat low. Atmospheric Science Letters, 11(4), 255-264. doi:10.1002/asl.284

Liu, X., Xie, X., Guo, Z., Yin, Z. Y., & Chen, G. (2022). Model-based distinct characteristics and mechanisms of orbital-scale precipitation δ18O variations in Asian monsoon and arid regions during late Quaternary. National Science Review.

Messori, G., Gaetani, M., Zhang, Q., Zhang, Q., & Pausata, F. S. R. (2018). The water cycle of the mid-Holocene West African monsoon: The role of vegetation and dust emission changes. International Journal of Climatology, 39(4), 1927-1939. doi:10.1002/joc.5924

Ngoungue Langue, C. G., Lavaysse, C., Vrac, M., Peyrillé, P., & Flamant, C. (2021). Seasonal forecasts of the Saharan heat low characteristics: a multi-model assessment. Weather and Climate Dynamics, 2(3), 893-912. doi:10.5194/wcd-2-893-2021

Nicholson, S. E. (2009). On the factors modulating the intensity of the tropical rainbelt over West Africa. International Journal of Climatology, 29(5), 673-689. doi:10.1002/joc.1702

Nicholson, S. E., & Klotter, D. (2020). The Tropical Easterly Jet over Africa, its representation in six reanalysis products, and its association with Sahel rainfall. International Journal of Climatology, 41(1), 328-347. doi:10.1002/joc.6623

Ohgaito, R., Yamamoto, A., Hajima, T., O'ishi, R., Abe, M., Tatebe, H., ... & Kawamiya, M. (2021). PMIP4 experiments using MIROC-ES2L Earth system model. Geoscientific Model Development, 14(2), 1195-1217.

O'Ishi, R., & Abe-Ouchi, A. (2011). Polar amplification in the mid-Holocene derived from dynamical vegetation change with a GCM. Geophysical Research Letters, 38(14), n/a-n/a. doi:10.1029/2011gl048001

Ohgaito, R., Yamamoto, A., Hajima, T., O'Ishi, R., Abe, M., Tatebe, H., . . . Kawamiya, M. (2021). PMIP4 experiments using MIROC-ES2L Earth system model. Geoscientific Model Development, 14(2), 1195-1217. doi:10.5194/gmd-14-1195-2021

Okazaki, A., & Yoshimura, K. (2019). Global Evaluation of Proxy System Models for Stable Water Isotopes With Realistic Atmospheric Forcing. Journal of Geophysical Research: Atmospheres, 124(16), 8972-8993. doi:10.1029/2018jd029463

Otto-Bliesner, B. L., Braconnot, P., Harrison, S. P., Lunt, D. J., Abe-Ouchi, A., Albani, S., . . . Zhang, Q. (2017). The PMIP4 contribution to CMIP6 – Part 2: Two interglacials, scientific objective and experimental design for Holocene and Last Interglacial simulations. Geoscientific Model Development, 10(11), 3979-4003. doi:10.5194/gmd-10-3979-2017

Perez-Sanz, A., Li, G., González-Sampériz, P., & Harrison, S. P. (2014). Evaluation of modern and mid-Holocene seasonal precipitation of the Mediterranean and northern Africa in the CMIP5 simulations. Climate of the Past, 10(2), 551-568. doi:10.5194/cp-10-551-2014

Quade, J., Dente, E., Armon, M., Ben Dor, Y., Morin, E., Adam, O., & Enzel, Y. (2018). Megalakes in the Sahara? A Review. Quaternary Research, 90(2), 253-275. doi:10.1017/qua.2018.46

Risi, C., Bony, S., Vimeux, F., & Jouzel, J. (2010). Water-stable isotopes in the LMDZ4 general circulation model: Model evaluation for present-day and past climates and applications to climatic interpretations of tropical isotopic records. 115(D12). doi:https://doi.org/10.1029/2009JD013255

Steinig, S., Harlaß, J., Park, W. et al. Sahel rainfall strength and onset improvements due to more realistic Atlantic cold tongue development in a climate model. Sci Rep 8, 2569 (2018). https://doi.org/10.1038/s41598-018-20904-1

Specht, N. F., Claussen, M., & Kleinen, T. (2022). Simulated range of mid-Holocene precipitation changes from extended lakes and wetlands over North Africa. Climate of the Past, 18(5), 1035-1046. doi:10.5194/cp-18-1035-2022

Sturm, C., Zhang, Q., & Noone, D. (2010). An introduction to stable water isotopes in climate models: benefits of forward proxy modelling for paleoclimatology. Clim. Past, 6(1), 115-129. doi:10.5194/cp-6-115-2010

Sundqvist, H. S., Kaufman, D. S., McKay, N. P., Balascio, N. L., Briner, J. P., Cwynar, L. C., . . . Viau, A. E. (2014). Arctic Holocene proxy climate database – new approaches to assessing geochronological accuracy and encoding climate variables. Clim. Past, 10(4), 1605-1631. doi:10.5194/cp-10-1605-2014

Takata, K., Emori, S., & Watanabe, T. (2003). Development of the minimal advanced treatments of surface interaction and runoff. Global and planetary Change, 38(1-2), 209-222.

Tegen, I., Harrison, S. P., Kohfeld, K., Prentice, I. C., Coe, M., & Heimann, M. (2002). Impact of vegetation and preferential source areas on global dust aerosol: Results from a model study. Journal of Geophysical Research: Atmospheres, 107(D21), AAC 14-11-AAC 14-27. doi:10.1029/2001jd000963

Tharammal, T., Bala, G., Paul, A., Noone, D., Contreras-Rosales, A., & Thirumalai, K. (2021). Orbitally driven evolution of Asian monsoon and stable water isotope ratios during the Holocene: Isotope-enabled climate model simulations and proxy data comparisons. Quaternary Science Reviews,252, 106743.

Thiery, W., Davin, E. L., Panitz, H.-J., Demuzere, M., Lhermitte, S., & van Lipzig, N. (2015). The Impact of the African Great Lakes on the Regional Climate. Journal of Climate, 28(10), 4061-4085. doi:10.1175/jcli-d-14-00565.1

Thompson, A. J., Zhu, J., Poulsen, C. J., Tierney, J. E., & Skinner, C. B. (2022). Northern Hemisphere vegetation change drives a Holocene thermal maximum. Sci Adv, 8(15), eabj6535. doi:10.1126/sciadv.abj6535

Thorncroft, C. D., Nguyen, H., Zhang, C., & Peyrillé, P. (2011). Annual cycle of the West African monsoon: regional circulations and associated water vapour transport. Quarterly Journal of the Royal Meteorological Society, 137(654), 129-147. doi:10.1002/qj.728

Tootchi, A., Jost, A., & Ducharne, A. (2019). Multi-source global wetland maps combining surface water imagery and groundwater constraints. Earth System Science Data, 11(1), 189-220. doi:10.5194/essd-11-189-2019

Watanabe, M., Suzuki, T., O'ishi, R., Komuro, Y., Watanabe, S., Emori, S., . . . Kimoto, M. (2010). Improved Climate Simulation by MIROC5: Mean States, Variability, and Climate Sensitivity. Journal of Climate, 23(23), 6312-6335. doi:10.1175/2010jcli3679.1

Supplement of

Contribution of Lakes in Sustaining Greening of the Sahara during the Mid-Holocene

Yuheng Li[1], Kanon Kino[1], Alexandre Cauquoin[2] and Taikan Oki[1]

[1]Department of Civil Engineering, Graduate School of Engineering, the University of Tokyo, Tokyo, Japan.

[2]Institute of Industrial Science, The University of Tokyo, Kashiwa, Japan.

Correspondence to: Yuheng Li (yuheng@rainbow.iis.u-tokyo.ac.jp)

Contents of this file

Table S1

Figures S1 to S13

删除了: 8

Table S1.

Table S1 Lake Maps

Lake Maps	Spatial resolution of original lake reconstruction	Description	Reference
LK_98 (small-lake map)	160 km	Holocene small-lake fraction derived from paleo-ecological reconstructions	(Hoelzmann, Jolly et al., 1998)
LK_02 (potential maximum-lake map)	160 km	mid-Holocene maximum-lake fraction derived using the hydrological routing algorithm (HYDRA)	(Tegen, Harrison et al., 2002)
LK1, LK2, LK3, LK4	15 arc-second	RFM2 model results on the wetlands of North Africa during the mid-Holocene corresponding to the four different rainfall types (LK1-4). The LK1 and LK2 are derived from IPSL-CM6A-LR mid-Holocene simulation; LK3 and LK4 are based on EC-Earth mid-Holocene simulation	(Chen, Ciais et al., 2021)

Considering the different spatial resolutions of the above datasets, the input lake maps have been upscaled into T42 spatial resolutions by calculating the lake area grid proportion in each T42 grid in North Africa Areas. Besides, this study used the same LK_98 and LK_02 maps as that of Specht, Claussen et al. (2022), which have been published in *http://hdl.handle.net/21.11116/0000-0009-63B5-B*.

删除了: MH_98
删除了: MH_02
删除了: MH1
删除了: MH2
删除了: MH
删除了: MH3
删除了: MH4
删除了: MH1
删除了: MH2
删除了: MH3
删除了: MH4
删除了: MH_98
删除了: MH_02

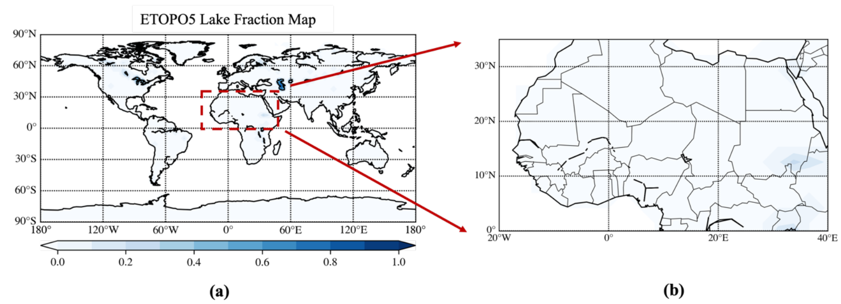

Figure S1. The (a) global prescribed lake map for mid-Holocene (MH) and pre-industrial (PI) reference experiments (ETOPO5). (b) Focus over North Africa.

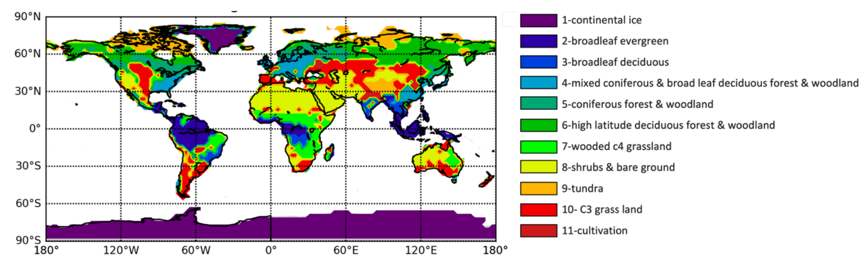

Figure S2. Vegetation type distribution map for all the experiments.

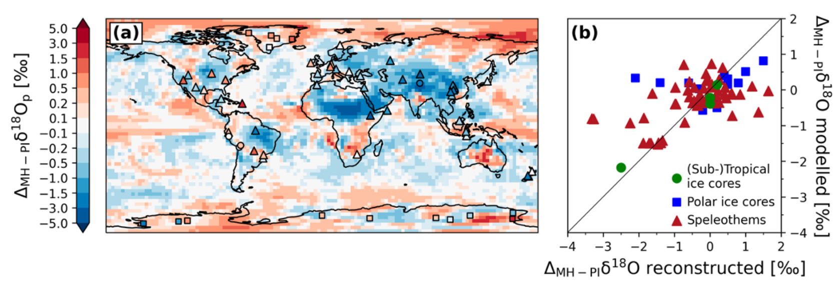

Figure S3. Isotope model-data comparison for the reference mid-Holocene simulation. The subplot (a) shows the simulated global pattern of annual mean $\delta^{18}O_p$ changes in precipitation between the MH_{ref} and PI_{ref} climate (background colors) and the observed $\delta^{18}O$ changes in polar (squares) and (sub)tropical (dots) ice cores and in calcite speleothems. The subplot (b) is a scatter plot showing a comparison of observed δ18O changes from ice cores and speleothems vs. with simulated MH–PI δ18Op anomalies at the same location.

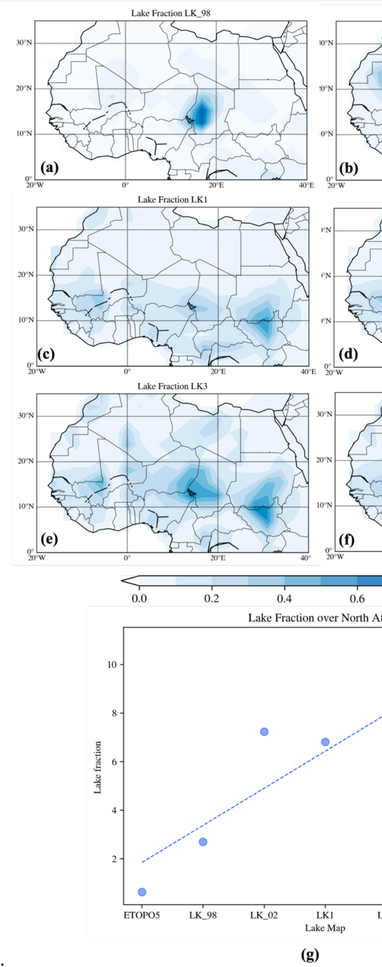

删除了:

删除了: The mid-Holocene (MH) lake maps in northern Africa used in this study: (a) the small lake map derived by (Hoelzmann, Jolly et al., 1998) used for the MH_C experiments, (b) the maximum lake map derived by Tegen, Harrison et al. (2002) used for the MH_{WC} experiments, (c)-(f) the potential lake maps derived by Chen, Ciais et al. (2021) corresponding to four different types of precipitation, used for the MH_{WCE1}, MH_{WCE2}, MH_{WCE3} and MH_{WCE4} experiments, respectively. The lake maps differences mainly come from the western Sahara lakes, Megalake Chad and eastern lakes in South Sudan (between 0° -20° N). (g) The

删除了: fraction (circle size) of all the prescribed lakes experiments compared with the present global land surface areas (1.48 ×10^8 km2).

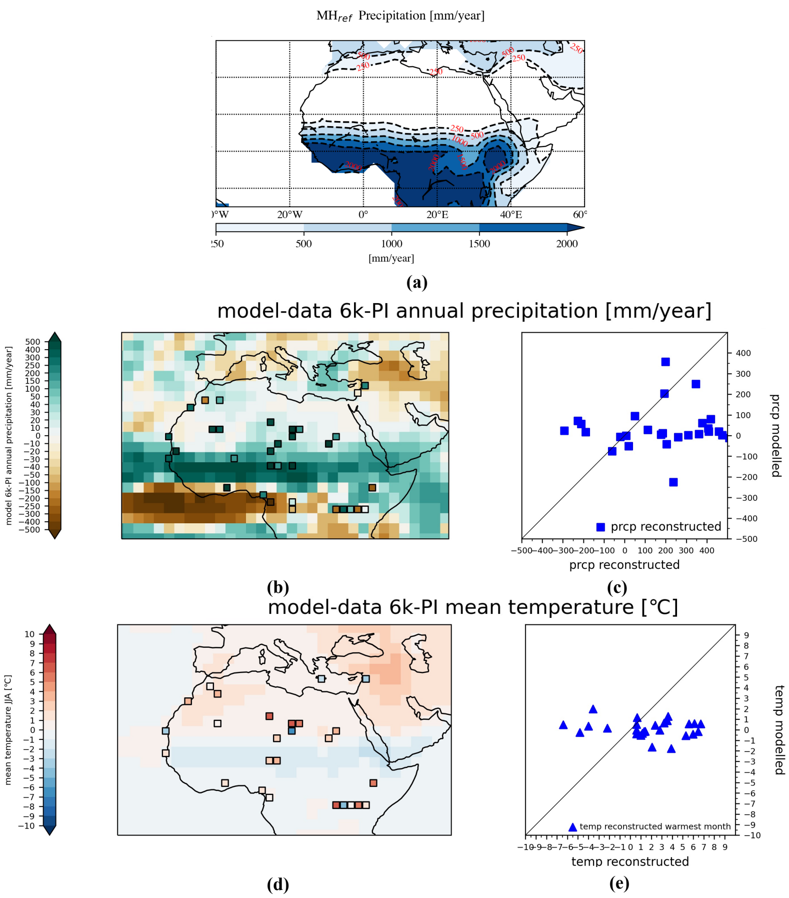

Figure S4. Precipitation and temperature model-data comparison for the reference mid-Holocene simulation in North Africa. (a) The spatial annual precipitation for MH$_{ref}$. (b) shows the simulated global pattern of annual mean precipitation between the MH$_{ref}$ and PI$_{ref}$ climate (background colors) and the observed annual mean precipitation changes (squares) between MH$_{ref}$ and the present climate. (c) is a scatter plot showing a comparison of observed precipitation changes with simulated precipitation anomalies at the same location. (d) and (e) are the same as (b) and (c) but for the seasonal mean temperature model [Summer (JJA)]-data [warmest month] comparison.

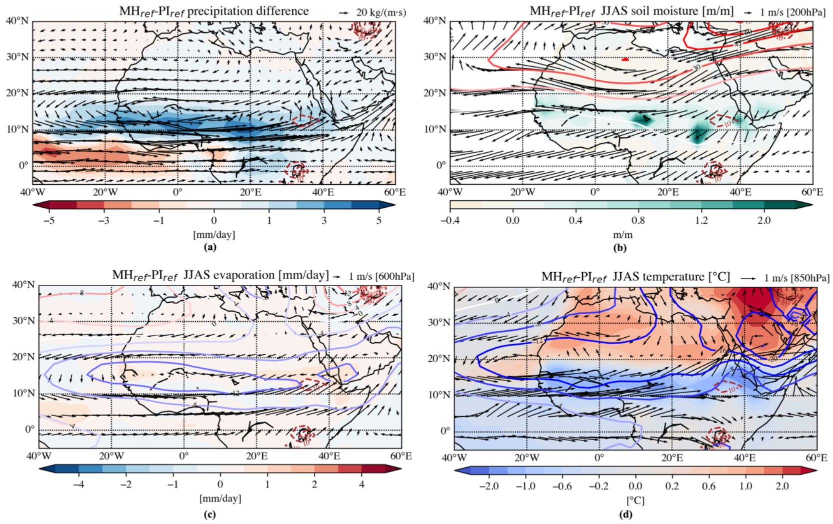

***Figure S5*.** The simulated climatological mean anomalies between MHref and PIref in JJAS: (a) precipitation (shades) and the integrated vapor transportation anomalies (IVT; arrows); (b) soil moisture (shades) with 200 hPa wind (arrows) and geopotential height (contours); (c) evaporation (shades) with and 600 hPa horizontal wind (arrows) and geopotential height (contours); (d) surface temperature (shades) with 850 hPa horizontal wind (arrows), and geopotential height (contours). For (a)-(d), the lake fraction [%] contours of the respective lake sensitivity experiment are shown with the red dashed lines, and the respective reference scale for the arrow is shown at the right top of each panel.

删除了: ***4***

删除了: ↵

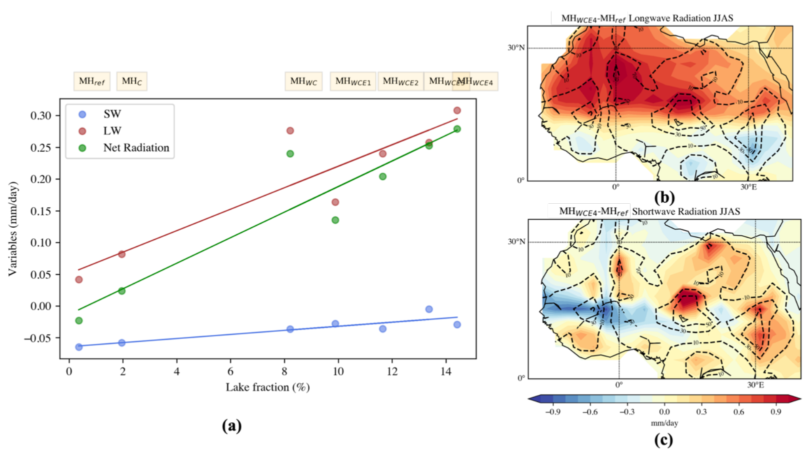

Figure S6. (a) Statistical relationship between regionally averaged radiation variables anomaly and averaged grid lake fraction over Northern Africa (20°W–40°E, 0–35°N) for MH lake experiments anomalies (relative to PI_{ref}) on the annual (circle) averages. The radiation variables include net surface shortwave radiation (blue), net surface longwave radiation (red), and net radiation (green). Simulated mid-Holocene climatological JJAS mean anomalies MH_{WCE4} with respect to MH_{ref}: (b) net surface longwave radiation (shades), (c) net surface shortwave radiation (shades). For maps (b) and (c), The lake fraction [%] contours of the respective lake sensitivity experiment are shown with the black dashed lines. All the radiations units has been transferred from [W/m^2] to [mm/day] based on the equation: $W/m^2 = 1000(kg/m^3) \times 2.5\times10^6(J/kg) \times 1mm/day\ (1/86400)(day/s) \times (1/1000)(mm/m)$.

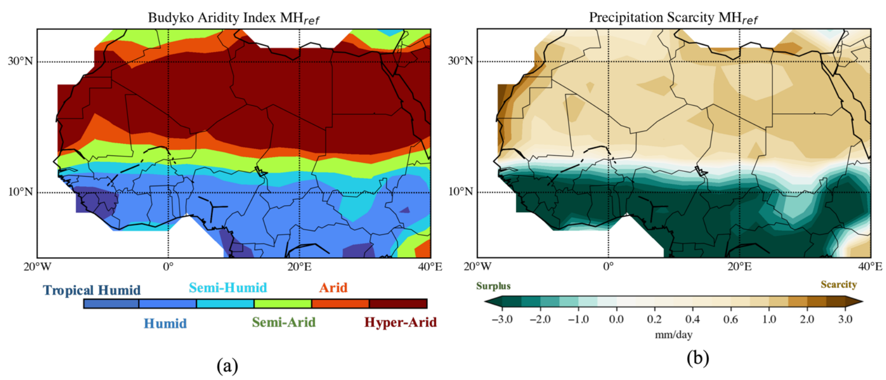

Figure S7, (a) The spatial distribution of six climate regions and (b) The spatial distribution of precipitation scarcity and precipitation surplus over Northern Africa for MH_{ref} experiments.

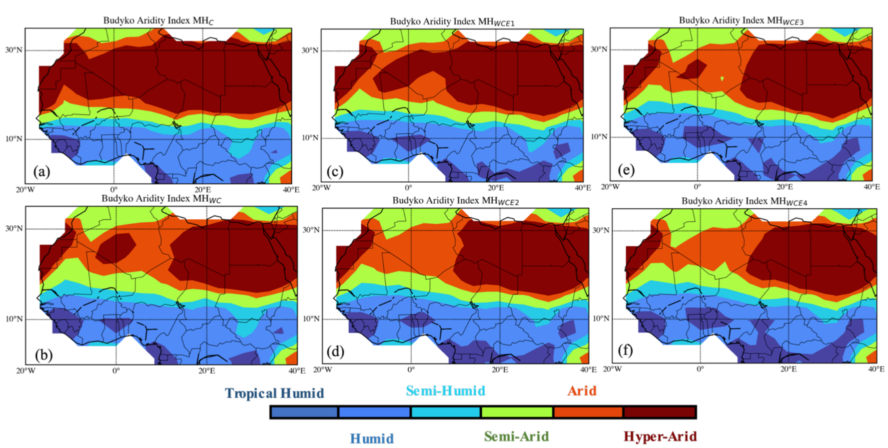

Figure S8, The spatial distribution of six climate regions for MH_C, MH_{WC}, MH_{WCE1}, MH_{WCE2}, MH_{WCE3}, and MH_{WCE4} experiments. The climate zones are classified with Budyko Aridity index (I) and precipitation (P) in Northern Africa: Tropical Humid ($I \leqslant 0.7$ and $P > 2,000$ mm/yr), Humid ($0.7 < I \leqslant$

删除了: ***5***

删除了: The spatial distribution of precipitation scarcity and precipitation surplus over Northern Africa

删除了: the spatial distribution of six climate regions for MH_{ref} experiments

删除了: ***6***

1.2), Semi-Humid (1.2 < I ⩽ 2.0), Semi-Arid (2.0 < I ⩽ 4.0), Arid (4.0 < I ⩽ 6.0) and Hyper-Arid (6.0 < I). For Budyko Aridity index calculation, see the main text in method detail.

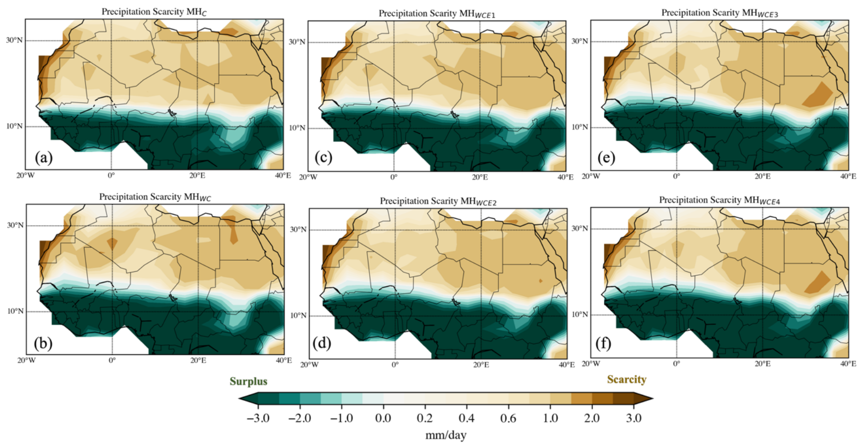

Figure S9, The spatial distribution of precipitation scarcity and precipitation surplus over Northern Africa for all the mid-Holocene experiments.

删除了: *7*

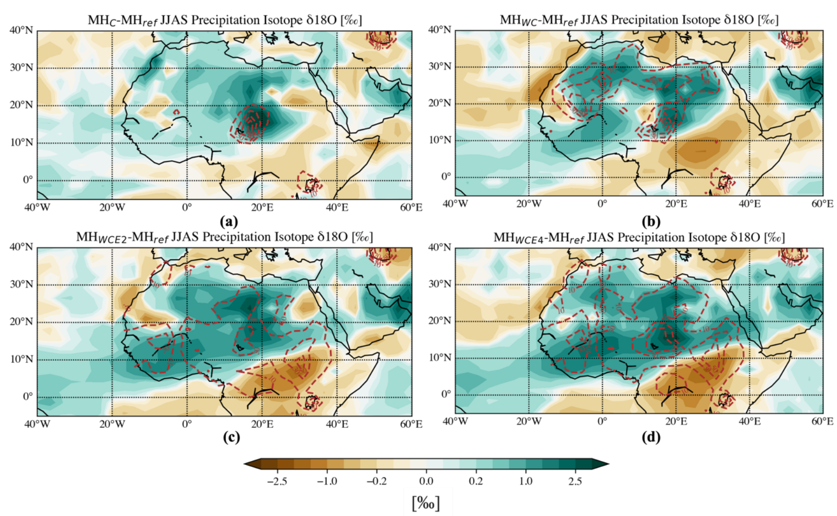

Figure S10, Changes in the stable isotope ratio $\delta^{18}O$ [‰] in precipitation for our mid-Holocene sensitivity experiments relative to MH_{ref}: (a) the climatological δ18O anomaly for MH_98 experiments. (b), (c) and (d) are the same as (a) but for the MH_{WC}, MH_{WCE2} and MH_{WCE4} experiments, respectively. For (a)-(d), the lake fraction [%] contours of the respective lake sensitivity experiment are shown with the red dashed lines.

删除了: *8*

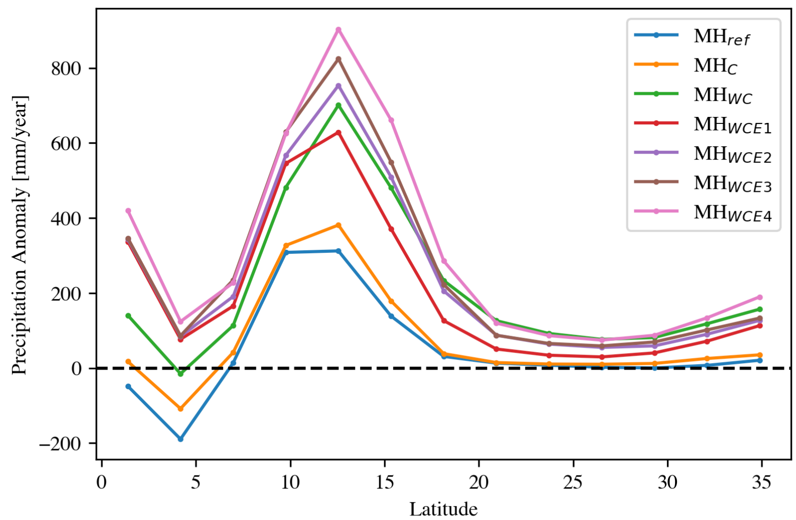

Figure 11. Zonal means, over "North Africa" land [-20°W-35°E, 0-35°N] of annual precipitation anomalies of the mid-Holocene experiments with respect to PI_{ref}.

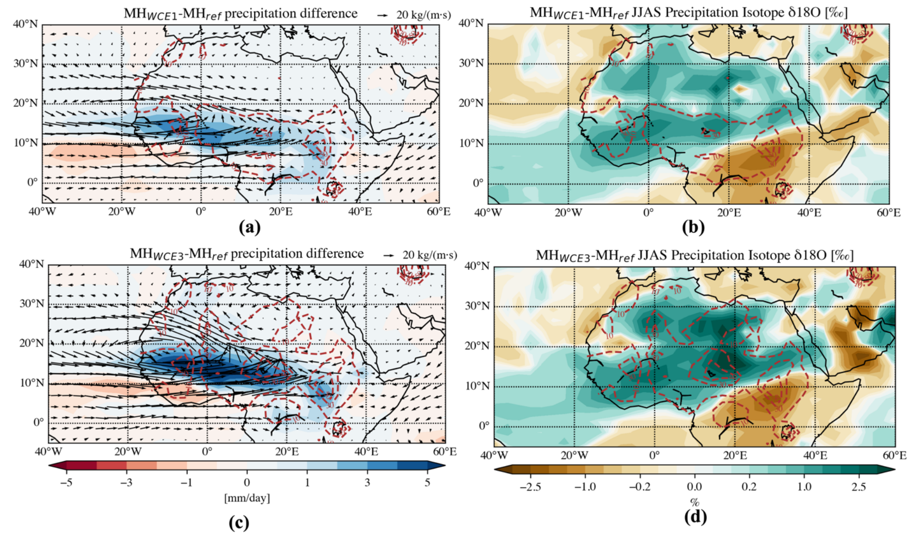

Figure S12. Anomalies relative to MH$_{ref}$ in simulated mid-Holocene climatological summer mean (June-July-August-September, JJAS) precipitation (shades) and integrated vapor transportation (IVT; arrows) for (a) MH$_{WCE1}$ and (c) MH$_{WCE3}$ experiments, respectively. Changes in the stable isotope ratio δ^{18}O [‰] in precipitation for our mid-Holocene sensitivity experiments relative to MH$_{ref}$: (a) the climatological δ18O anomaly for MH$_{WCE1}$ experiments. (b) is the same as (a) but for the MH$_{WCE3}$. For (a)-(d), the lake fraction [%] contours of the respective lake sensitivity experiment are shown with the red dashed lines (contour spacing: 10%-30%-50%-70%-100%), and the respective reference scale for the arrow is shown at the right top of each panel.

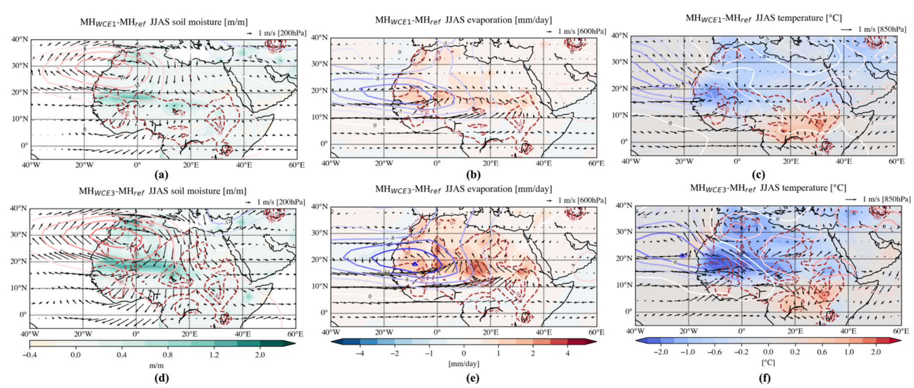

Figure S13. Simulated mid-Holocene climatological JJAS mean anomalies with respect to MH$_{ref}$: (a) soil moisture (shades) with 200 hPa wind (arrows) and geopotential height (contours), (b) evaporation (shades) with 600 hPa horizontal wind (arrows) and geopotential height (contours) and (c) surface temperature (shades) with 850 hPa horizontal wind (arrows), and geopotential height (contours) for MH_{WCE1} experiment. Map (d), (g) and (f) are the same as (a), (b) and (c), respectively, but for MH_{WCE3} experiment. For all the maps, the lake fraction [%] contours of the respective lake sensitivity experiment are shown with the red dashed lines, and the respective reference scale for the arrow is shown at the right top of each panel.